Astron. Astrophys. 331, 601–611 (1998)

ASTRONOMY
AND
ASTROPHYSICS

X-ray emission from NGC 4321 (M 100): detection of supernova 1979C

S. Immler, W. Pietsch, and B. Aschenbach

Max-Planck-Institut für extraterrestrische Physik, Postfach 1603, D-85740 Garching, Germany

Received 26 August 1997 / Accepted 14 November 1997

Abstract. In a 42.8 ks ROSAT HRI X-ray observation of the spiral galaxy NGC 4321 (M 100) X-ray emission from the supernova 1979C is discovered, sixteen years after its outburst, with an (0.1–2.4 keV) X-ray luminosity of $L_{\rm x} = 1.0 \times 10^{39}$ erg s^{-1}. No X-ray emission is observed from the three other historical supernovae in NGC 4321 (SN 1901B, SN 1914A and SN 1959E).

In addition to SN 1979C, seven X-ray point sources are detected inside the D_{25} ellipse of the galaxy, with luminosities ranging from 4.2×10^{38} to 6.5×10^{39} erg s^{-1}. Apart from two bright sources in the nuclear region of NGC 4321, none of the other point-like X-ray sources show any time variability over the observation period. An unresolved diffuse emission component fills the entire optical extent of the galaxy. The total luminosity of the diffuse component is 3.5×10^{40} erg s^{-1}. Point sources contribute 1.4×10^{40} erg s^{-1} to the total luminosity of 5.5×10^{40} erg s^{-1}.

Three archival *Einstein* HRI observations of NGC 4321 were merged into a single 41.3 ks observation. Six point-like X-ray sources are detected inside the D_{25} ellipse of NGC 4321 with *Einstein* (0.1–4.5 keV) luminosities in the range 1.1 – 5.1×10^{39}erg s^{-1}. Three of the sources coincide with the positions of ROSAT sources (the two bulge sources and a southern interarm source). Comparison of the ROSAT and *Einstein* luminosities show that the sources are variable. *Einstein* upper limits are evaluated at the positions of all other ROSAT sources and historical supernovae in NGC 4321.

Key words: galaxies: individual: NGC 4321 (=M 100) – supernovae: individual: SN 1979C (M 100) – ISM: supernova remnants – X-rays: galaxies

1. Introduction

The weakly-barred spiral galaxy NGC 4321 (M 100, type SAB(s)bc, de Vaucouleurs et al. 1991) is the brightest member of the Virgo S cluster at a distance of 17.1 Mpc (Freedman et al. 1994). NGC 4321 is an ideal target for studying the X-ray emission components of late-type spiral galaxies since it is seen almost face-on (inclination $i = 27^\circ$) and has a large D_{25} diameter ($6\farcm9$, de Vaucouleurs et al. 1991). It lies in a direction with a relatively low Galactic hydrogen column density ($N_{\rm H} = 2.3 \times 10^{20}$ cm^{-2}, Dickey & Lockman 1990). General properties of NGC 4321 are summarised in Table 1.

An interesting aspect of studying NGC 4321 in the X-ray regime is the unusually high number of supernovae (SNe) recorded this century (SN 1901B, SN 1914A, SN 1959E, SN 1979C). The last of the four known SNe in NGC 4321 (SN 1979C, type II$_{\rm L}$) was optically very bright near maximum light on April 19, 1979 ($m_{\rm B}^{\rm max} \leq 12$, Johnson 1979), and reached a maximum 6 cm radio flux density of 8.3 mJy one year after the explosion (for a review of the radio characteristics of SN 1979C cf. Weiler et al. 1986 and 1991).

Radio-bright SNe are promising targets for X-ray investigations since both the radio and X-ray emission processes are considered to be linked to the interaction between the SN ejecta and the circumstellar matter. The ROSAT instruments are well suited to searching for X-ray emission from SNe in nearby galaxies, on account of both their high sensitivity in the soft (0.1–2.4 keV) X-ray band, where the peak of the X-ray emission is expected, and their high spatial resolution ($\sim 5''$ for the HRI and $\sim 25''$ for the PSPC). Previous ROSAT detections of SNe in nearby galaxies include the type II SNe SN 1978K in NGC 1313, SN 1980K in NGC 6946, SN 1986J in NGC 891, SN 1987A in the LMC, SN 1988Z in MCG+03-28-022, SN 1993J in NGC 3031 and SN 1995N in MCG-2-38-017, with X-ray luminosities in the range 10^{35} – 10^{41} erg s^{-1} (cf. Schlegel 1995 for a review of X-ray emission from SNe).

A $\sim$ 13 ks *Einstein* HRI observation of NGC 4321 from December 1979, 239 days after SN 1979C's outburst led to the discovery of two bright ($\sim 10^{40}$ erg s^{-1}) sources in NGC 4321, one at the center of the galaxy and one in the northern spiral arm. No significant X-ray emission was detected from the four SNe known in NGC 4321 (Palumbo et al. 1981).

In this paper we add to the ROSAT detections of X-ray bright type II SNe in nearby galaxies by the discovery of SN 1979C with the ROSAT HRI, and give upper limits for SN 1901B,

Send offprint requests to: S. Immler, (simmler@mpe.mpg.de)

Table 1. Parameters of NGC 4321

Parameter	Value	Ref.
Type	SAB(s)bc	[a]
Position of center (J2000) .	R.A. $12^h22^m55^s.2$	[b]
.....	Dec. $+15°49'08''.0$	[b]
Distance	17.1 ± 1.8 Mpc	[c]
.....	(hence $1' \widehat{=} 5.0$ kpc)	
Galactic foreground N_H	2.3×10^{20} cm^{-2}	[d]
Inclination	27°	[a]
Position angle of major axis	$153° \pm 1°$	[e]
D_{25} diameter	$6'.9$	[a]

[a] de Vaucouleurs et al. (1991)
[b] SIMBAD data base
[c] Freedman et al. (1994)
[d] Dickey & Lockman (1990)
[e] Knapen et al. (1993)

SN 1914A and SN 1959E. A list of point-like X-ray sources in the HRI field of view centered on NGC 4321 is presented. In addition to the point sources, residual diffuse emission is visible over the entire optical extent of the galaxy and the possible origin of this diffuse X-ray emission is discussed.

We analysed three archival *Einstein* HRI observations totalling $\sim$ 41 ks integration time and compiled a list of point sources to study the long term variability of the X-ray sources. *Einstein* IPC observations of NGC 4321 have not been used because of their poor spatial resolution ($\sim 1'$).

2. Observation and data reduction

NGC 4321 was observed with the ROSAT HRI for 42.8 ks in 20 observation intervals (OBIs) from June 5 to 28, 1995. For a description of the ROSAT satellite and the detectors aboard cf. Trümper (1983).

The observation reaches a point source detection limit of $L_x \sim 1.8 \times 10^{38}$ erg s^{-1}, assuming a 5 keV thermal bremsstrahlung spectrum, a foreground column density of $N_H = 2.3 \times 10^{20}$ cm^{-2} and a distance of 17.1 Mpc.

Attitude solutions of ROSAT pointings derived from the Standard Analysis Software System (SASS, Voges et al. 1992), show residual errors of $6''$ (boresight error). To improve the attitude solution we used ten bright point sources visible in each OBI, to align each of the different OBIs with respect to the first. No offset is seen to exceed $6''.3$. The resulting attitude solution was tested by comparing the positions of X-ray point sources and 12 possible optical counterparts suggested by the APM finding charts (Irwin et al. 1994). By shifting the X-ray coordinates $3''.3$ to the south and $0''.8$ to the west a close accordance of X-ray and optical sources could be established (remaining systematic error $\sim 3''.9$).

The corrected center of the HRI field is at R.A. = $12^h22^m55^s.1$ and Dec. = $+15°49'08''.7$ (J2000).

Data reduction was performed with the EXSAS software package (Zimmermann et al. 1994). The applied analysis procedures are described in Vogler & Pietsch (1996). In order to reduce the background due to UV emission and cosmic rays we only used HRI raw channels 2–8.

Fig. 1 shows the inner $8'.5 \times 8'.5$ field of the HRI image in contour representation. The D_{25} ellipse indicates the optical extent of NGC 4321. Positions of detected X-ray sources are enclosed by squares and numbered according to the HRI source list (Table 2), positions of the known SNe are marked with crosses.

Archival *Einstein* observations of NGC 4321 were analysed to supplement the ROSAT HRI data. Three *Einstein* HRI observations from June 7, 1979 ($\sim$ 4 ks), December 10, 1979 ($\sim$ 13 ks), and July 1–2, 1980 ($\sim$ 24 ks), were merged into a single $\sim$ 41 ks observation. A local source detection algorithm was applied to an $\sim 18' \times 18'$ image (where the three observations overlap) of $8''$ pixel size, centered on NGC 4321. Background corrected count rates were evaluated within circles of $18''$ radius (corresponding to the standard *Einstein* HRI detection cell, Harris 1984) at the positions of both the *Einstein* sources detected with a maximum likelihood $L \geq 8$, the ROSAT HRI sources, and the historical SNe. Fig. 2 shows the *Einstein* HRI observation in contour representation. The *Einstein* sources are marked with diamond symbols and numbered according to the source list (Table 3). Positions of ROSAT sources and SNe are indicated as in Fig. 1.

3. Results

3.1. Point sources

Selecting point-like sources with a of likelihood $L \geq 8$ (corresponding to a Gaussian significance of 3.6σ) leads to a total of 33 X-ray sources in the $34' \times 34'$ ROSAT HRI field of view, eight of which are within the D_{25} ellipse of NGC 4321 (H17–H19, H21–H25). The X-ray properties of the sources are summarised in Table 2: source number (col. 1, 'H' denotes HRI), right ascension and declination (col. 2, 3), 90% confidence error radius of the source position (col. 4, including $3''.9$ systematic error for the attitude solution), likelihood of existence (col. 5), net counts and error in the 0.1–2.4 keV ROSAT band (col. 6), count rates and error, corrected for vignetting and deadtime (col. 7), and fluxes in the ROSAT band (col. 8). Fluxes were computed assuming a galactic column density of $N_H = 2.3 \times 10^{20}$ cm^{-2} (Dickey & Lockman 1990) and a 5 keV thermal bremsstrahlung spectrum. This is a typical spectrum of point sources in normal galaxies derived from *Einstein* observations (Fabbiano 1989). ROSAT results for point sources in normal galaxies show that they tend to have spectra of somewhat lower temperatures ($\sim$ 1 keV). Since the difference of the energy conversion factors for a 1 keV and a 5 keV thermal bremsstrahlung spectrum is less than $\sim 5\%$, we assume a 5 keV thermal bremsstrahlung spectrum for all point sources.

The luminosities of the eight sources inside the D_{25} ellipse of NGC 4321 lie in the range 4.2×10^{38} to 6.5×10^{39} erg s^{-1}.

The strongest source (H23) coincides with the optical nucleus of NGC 4321. It is the only source flagged as extended by the detection algorithm (likelihood of extent $L_{ext} = 82.4$), with

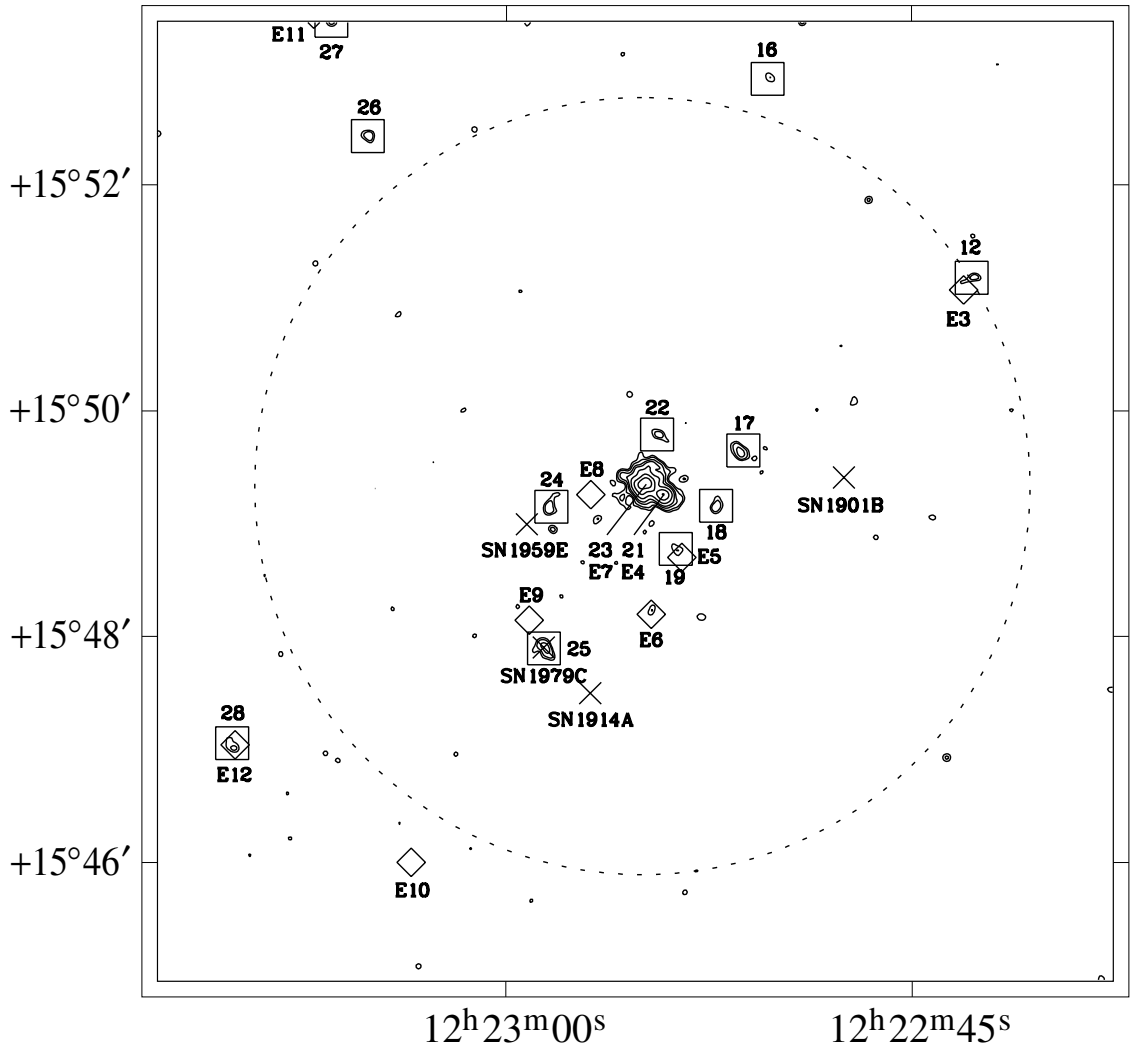

Fig. 1. Contours of X-ray emission from NGC 4321 in the ROSAT HRI band (0.1–2.4 keV). The D_{25} diameter of the galaxy is indicated by the dotted circle. The image was constructed with a pixel size of $1''$ and smoothed with a Gaussian filter of $4\farcs7$ (FWHM). HRI sources with L $\geq$ 8 are enclosed by boxes and labelled according to the ROSAT source list (Table 2), *Einstein* sources (L $\geq$ 8, cf. Table 3) are indicated by diamonds. The positions of SNe are marked with crosses. X-ray contour levels are $3, 4, 6, 8, 12, 18$ and 24σ above the mean background rate of 3.8×10^{-3} cts s^{-1} arcmin^{-2}. $1\sigma \mathrel{\widehat{=}} 3.3 \times 10^{-3}$ cts s^{-1} arcmin^{-2}.

a FWHM of $9\farcs8$. Another bright point source is found close to the nucleus (H21, 3.0×10^{39} erg s^{-1}, $15''$ offset).

The analysis of the merged *Einstein* HRI observations leads to the detection of six sources with $L \geq 8$ inside the D_{25} ellipse of NGC 4321 and a total of 14 sources within the inner $\sim 18' \times 18'$, where the three *Einstein* HRI observations overlap. The brightest source in the *Einstein* observations (E15) is contained within the field of view of the 23.8 ks observation only. Background subtracted count rates were extracted from circles of radius $18''$ (corresponding to the *Einstein* HRI standard detection cell) at the positions of the *Einstein* sources. Count rates were converted to (0.1–4.5 keV) X-ray fluxes, assuming a 5 keV Raymond & Smith thermal plasma (absorbed by a hydrogen column density of $N_{\rm H} = 2.3 \times 10^{20}$ cm^{-2}), since the *Einstein* Observatory Revised User's Manual (Harris 1984) does not give energy conversion factors for thermal bremsstrahlung spectra. At the given high temperatures, however, the Raymond & Smith thermal plasma spectrum is dominated by continuum emission and the difference between a 5 keV thermal bremsstrahlung spectrum and a 5 keV Raymond & Smith spectrum is less than $\sim 5\%$.

Properties of the *Einstein* sources are given in Table 3: source designation (col. 1, 'E' denotes *Einstein*) and the name of the corresponding ROSAT source in cases where the positional deviation does not exceed $5''$, right ascension and declination (col. 2, 3), likelihood of existence (col. 4), net counts and statistical error in the 0.1–4.5 keV *Einstein* band (col. 5), count rates and error (col. 6) and fluxes in the *Einstein* band (col. 7). Col. 8 gives the (0.1–2.4 keV) fluxes for the ROSAT HRI observation, calculated from circles of radius $2.5\times$ the ROSAT HRI PSF, at the positions of each of the *Einstein* sources. Where an *Einstein* source was not detected in the ROSAT observation at

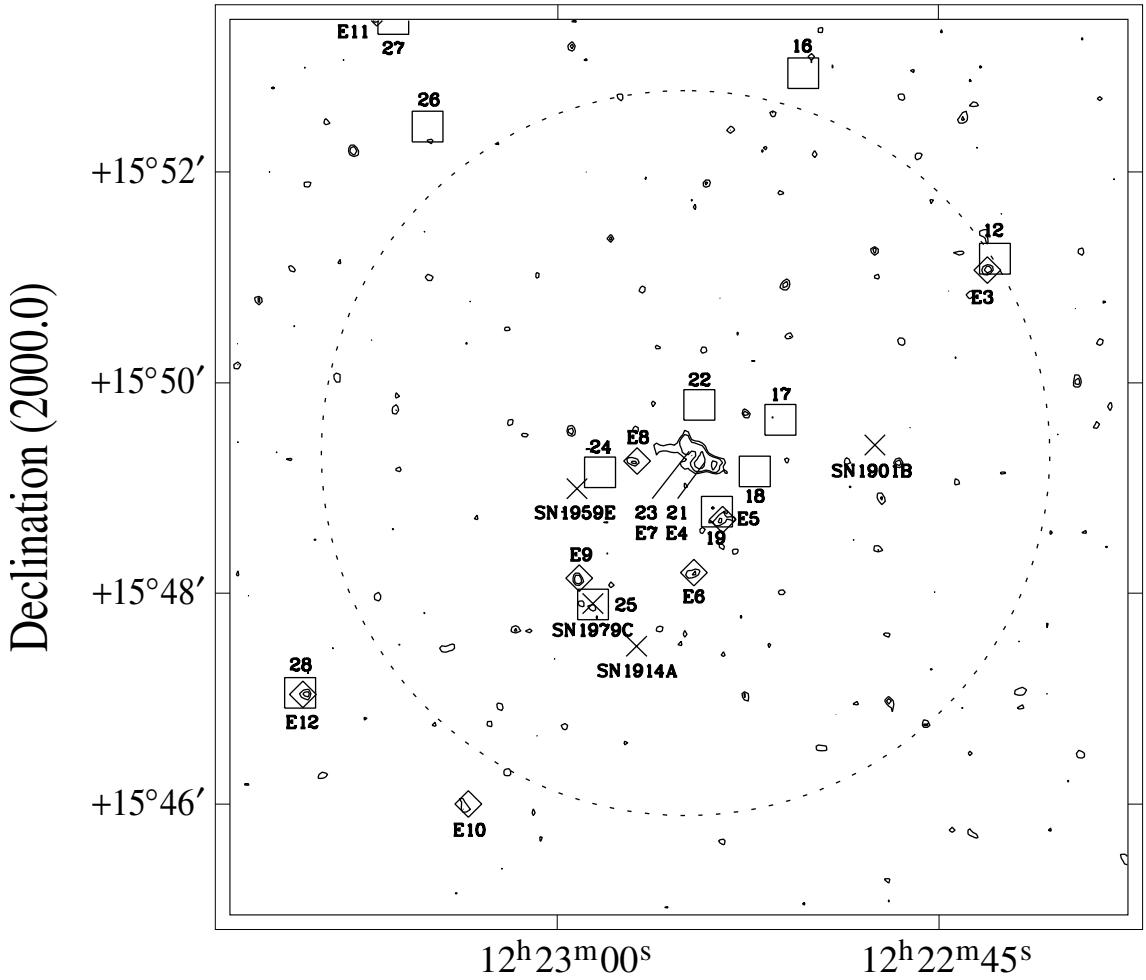

Fig. 2. Contours of X-ray emission from NGC 4321 in the *Einstein* HRI band (0.1–4.5 keV). X-ray contour levels (4.″7 FWHM) are $3, 4, 6$ and 8σ above the mean background rate (1.1×10^{-2} cts s^{-1} arcmin^{-2}, $1\sigma \mathrel{\widehat{=}} 7.1 \times 10^{-3}$ cts s^{-1} arcmin^{-2}). Same scale and source labelling as in Fig. 1.

the 3σ confidence level, a 3σ upper limit was calculated. Of the 15 detected *Einstein* sources eight point-like sources coincide with the positions of ROSAT sources to within $5''$.

Conversely, count rates, fluxes and 3σ upper limits (in the cases of non-detections) were evaluated at the positions of the ROSAT sources for the *Einstein* observations. Table 4 gives the ROSAT and *Einstein* fluxes and luminosities of the ROSAT HRI sources found inside the D_{25} ellipse of NGC 4321.

Although three ROSAT HRI point sources inside the D_{25} ellipse of NGC 4321 are detected in the *Einstein* HRI observation (H19 and the two nuclear sources H21 and H23), no X-ray emission is observed from the historical SNe. The results of the *Einstein* data analysis are discussed in Sect. 4.

3.2. Time variability study of point sources

A time variability study was performed for all sources found in the ROSAT HRI field of view. The 20 observation intervals (OBIs) were binned into 4 observation blocks corresponding to OBIs 1–5 (10.9 ks), 6–11 (9.5 ks), 12–16 (9.5 ks) and 17–20 (9.1 ks). A maximum likelihood search at the source positions given in Table 2 was performed for each of the four observation blocks, and vignetting and deadtime corrected count rates and errors within a cut radius of $1.5\times$ the FWHM of the PSF at these source positions were calculated. If a source was not detected with a likelihood L > 3.1 (corresponding to a Gaussian significance of 2σ), a 2σ upper limit to the count rate was calculated. χ^2 statistics were used for testing for any X-ray variability.

Only source H30 (outside the D_{25} radius of NGC 4321) shows any variation in count rate between observation blocks 1 and 4 (a factor of ~ 4.5). It is the second brightest source detected in the HRI field of view, with a flux of $F_{\rm x} = 1.9 \times 10^{-13}$ erg cm^{-2} s^{-1}. Comparisons with APM finding charts (Irwin et al. 1994) suggest an identification of H30 with a faint non-stellar object (offset $2.''5$, $m_{\rm B} = 17.54$, $m_{\rm R} = 16.38$, $m_{\rm B} - m_{\rm R} = 1.16$).

The sources in the nuclear region (H21, H23) show evidence for small variations in count rate during the observation of a

Table 2. ROSAT HRI X-ray sources detected in the $34' \times 34'$ field of view centered on NGC 4321

Source	R.A. (J2000) (^{h} ^{m} ^{s})	Dec. (J2000) ($^\circ$ $'$ $''$)	R_{err} ($''$)	Lik.	Net counts	Count rate (10^{-4} s^{-1})	F_x [a] (10^{-14} $\frac{erg}{cm^2 s}$)
(1)	(2)	(3)	(4)	(5)	(6)	(7)	(8)
H1	12 21 45.52	+15 49 21.8	15.3	10.8	51.9 ± 13.2	12.1 ± 3.1	5.1 ± 1.3
H2	12 22 01.45	+15 58 34.1	12.9	9.1	41.8 ± 11.5	9.8 ± 2.7	4.2 ± 1.1
H3	12 22 03.03	+15 53 43.6	10.3	8.0	28.9 ± 8.8	6.8 ± 2.1	2.9 ± 0.9
H4	12 22 14.34	+15 51 44.7	9.9	8.7	26.0 ± 7.7	6.1 ± 1.8	2.6 ± 0.8
H5	12 22 22.10	+15 39 48.8	7.6	20.1	44.9 ± 9.4	10.5 ± 2.2	4.4 ± 0.9
H6	12 22 24.62	+15 53 34.3	11.7	11.9	18.1 ± 5.5	4.2 ± 1.3	1.8 ± 0.6
H7	12 22 27.73	+15 58 14.4	8.4	12.4	26.4 ± 7.3	6.2 ± 1.7	2.6 ± 0.7
H8	12 22 30.61	+15 55 52.9	4.5	616.7	264.5 ± 16.9	61.8 ± 4.0	26.2 ± 1.8
H9	12 22 33.01	+15 37 55.4	5.7	66.3	89.6 ± 11.7	20.9 ± 2.7	8.9 ± 1.1
H10	12 22 33.33	+15 50 56.4	13.7	9.6	17.6 ± 5.5	4.1 ± 1.3	1.7 ± 0.6
H11	12 22 38.24	+15 55 52.4	8.2	21.0	23.2 ± 5.7	5.4 ± 1.3	2.3 ± 0.6
H12	12 22 42.75	+15 51 10.9	10.7	9.1	10.2 ± 3.8	2.4 ± 0.9	1.0 ± 0.4
H13	12 22 42.90	+15 44 04.4	6.0	59.4	42.5 ± 7.1	9.9 ± 1.7	4.2 ± 0.7
H14	12 22 43.72	+15 56 55.0	9.6	15.9	21.8 ± 5.8	5.1 ± 1.4	2.2 ± 0.6
H15	12 22 48.27	+15 43 08.5	7.7	30.4	28.0 ± 6.0	6.6 ± 1.4	2.8 ± 0.6
H16	12 22 50.31	+15 52 57.0	8.6	9.0	9.8 ± 3.6	2.3 ± 0.9	1.0 ± 0.4
H17	12 22 51.21	+15 49 39.0	10.2	20.3	35.9 ± 7.5	8.4 ± 1.8	3.6 ± 0.8
H18	12 22 52.21	+15 49 09.5	9.1	11.4	14.2 ± 4.6	3.3 ± 1.1	1.4 ± 0.5
H19	12 22 53.70	+15 48 46.5	9.9	8.7	12.0 ± 4.3	2.8 ± 1.0	1.2 ± 0.4
H20	12 22 53.88	+15 56 58.5	8.5	16.9	19.4 ± 5.3	4.5 ± 1.2	1.9 ± 0.5
H21	12 22 54.15	+15 49 14.5	5.2	135.8	87.5 ± 10.1	20.4 ± 2.4	8.6 ± 1.0
H22	12 22 54.40	+15 49 47.5	12.2	9.4	14.4 ± 4.8	3.4 ± 1.1	1.4 ± 0.5
H23	12 22 55.02	+15 49 22.0	5.0	241.5	187.4 ± 14.6	43.8 ± 3.4	18.6 ± 1.4
H24	12 22 58.29	+15 49 09.0	9.2	13.7	16.6 ± 4.9	3.9 ± 1.1	1.7 ± 0.5
H25	12 22 58.57	+15 47 53.5	8.1	23.2	29.5 ± 6.4	6.9 ± 1.5	2.9 ± 0.6
H26	12 23 05.09	+15 52 26.5	7.5	13.7	13.4 ± 4.2	3.1 ± 1.0	1.4 ± 0.4
H27	12 23 06.44	+15 53 28.0	10.3	8.6	11.3 ± 4.1	2.6 ± 1.0	1.1 ± 0.4
H28	12 23 10.10	+15 47 02.9	7.9	13.5	15.1 ± 4.6	3.5 ± 1.1	1.5 ± 0.5
H29	12 23 17.44	+15 44 44.9	13.2	8.9	15.7 ± 5.2	3.7 ± 1.2	1.6 ± 0.6
H30	12 23 30.92	+15 45 08.8	4.2	336.1	191.1 ± 14.7	44.7 ± 3.4	18.9 ± 1.4
H31	12 23 33.18	+15 38 29.8	5.6	109.3	147.5 ± 15.0	34.5 ± 3.5	14.6 ± 1.5
H32	12 23 36.44	+15 40 25.2	9.7	16.6	44.4 ± 10.0	10.4 ± 2.3	4.4 ± 1.0
H33	12 23 48.78	+15 59 31.6	16.0	12.5	57.8 ± 13.8	13.5 ± 3.2	5.7 ± 1.4

[a] Fluxes are computed applying a 5 keV thermal bremsstrahlung spectrum, assuming a hydrogen column density of $N_H = 2.3 \times 10^{20}$ cm^{-2}.

factor 1.7 and 1.4 respectively (reduced χ^2 = 1.17 and 1.24). Variations in count rate do not exceed the 2σ statistical error for any of the other sources.

3.3. Source H25: Detection of SN 1979C

Source H25 coincides with the position of SN 1979C. The offset between the corrected HRI position and the radio position of SN 1979C (R.A.(J2000) = $12^h22^m58^s.58$, Dec.(J2000) = $+15^\circ47'52''.7$, Penhallow 1980) is $2''.7$.

H25 is observed to have a count rate of 6.9×10^{-4} cts s^{-1}. The total source flux and luminosity are $F_x = 2.9 \times 10^{-14}$ erg cm^{-2} s^{-1} and $L_x = 1.0 \times 10^{39}$ erg s^{-1} respectively, for a 5 keV thermal bremsstrahlung spectrum. Assumption of a 1 keV thermal bremsstrahlung spectrum leads to an X-ray luminosity of 1.1×10^{39} erg s^{-1}.

The probability of a chance coincidence of H25 with a background AGN at a given flux of 2.9×10^{-14} erg cm^{-2} s^{-1} within a radius of $5''$ is 1×10^{-4} (using the ROSAT Medium Sensitivity Survey; Hasinger, Schmidt & Trümper 1991).

Although the source was not flagged as extended by the detection algorithm (cf. Table 2), a slight elongation is visible in the high-resolution HRI image (cf. Fig. 1). The direction of the elongation however, appears coaligned with the direction of the satellite 'wobble' motion, and this effect is also visible in sources H17 and H22. We therefore conclude that source H25 is not extended.

Fig. 3 shows the X-ray lightcurve of SN 1979C during the periods of the ROSAT observations (cf. Sect. 3.2). Time is given in days relative to the beginning of the observation. Count rate errors are statistical. The dotted line represents the mean count

Table 3. Properties of *Einstein* HRI X-ray sources detected in the inner $\sim 18' \times 18'$ field centered on NGC 4321

Source		R.A. (J2000) (^{h} ^{m} ^{s})	Dec. (J2000) ($^\circ$ $'$ $''$)	*Einstein* HRI Lik.	Net counts	Count rate (10^{-4} s^{-1})	F_x [a] (10^{-14} $\frac{erg}{cm^2 s}$)	ROSAT HRI F_x [b] (10^{-14} $\frac{erg}{cm^2 s}$)
(1)		(2)	(3)	(4)	(5)	(6)	(7)	(8)
E1	= H8	12 22 30.59	+15 55 44.6	32.8	58.6 ± 8.7	14.2 ± 2.1	18.2 ± 2.7	25.9 ± 1.7
E2		12 22 38.45	+15 43 20.0	9.5	12.7 ± 5.4	3.1 ± 1.3	4.0 ± 1.7	< 1.4
E3	= H12	12 22 43.08	+15 51 05.7	8.2	13.2 ± 5.4	3.2 ± 1.3	4.1 ± 1.7	1.0 ± 0.4
E4	= H21	12 22 53.82	+15 49 13.7	10.5	38.6 ± 7.4	9.4 ± 1.8	12.0 ± 2.3	8.6 ± 1.0
E5	= H19	12 22 54.64	+15 48 12.7	8.0	17.3 ± 5.8	4.2 ± 1.4	5.4 ± 1.8	1.2 ± 0.4
E6		12 22 54.65	+15 48 11.7	10.0	12.7 ± 5.4	3.1 ± 1.3	4.0 ± 1.7	1.4 ± 0.6
E7	= H23	12 22 54.65	+15 49 19.7	8.8	46.0 ± 7.9	11.1 ± 1.9	14.2 ± 2.4	18.4 ± 1.4
E8		12 22 56.85	+15 49 15.7	8.2	10.5 ± 5.2	2.5 ± 1.3	3.2 ± 1.7	< 0.9
E9		12 22 59.14	+15 48 07.7	8.2	12.8 ± 5.4	3.1 ± 1.3	4.0 ± 1.7	1.0 ± 0.5
E10		12 23 03.50	+15 45 59.7	8.2	13.9 ± 5.5	3.4 ± 1.3	4.4 ± 1.7	< 1.6
E11	= H27	12 23 07.00	+15 53 30.0	11.1	11.9 ± 5.3	2.9 ± 1.3	3.7 ± 1.7	1.1 ± 0.4
E12	= H28	12 23 10.01	+15 47 01.7	12.1	15.8 ± 5.7	3.8 ± 1.4	4.9 ± 1.8	1.5 ± 0.4
E13		12 23 16.52	+15 45 35.6	11.1	14.9 ± 5.6	3.6 ± 1.4	4.6 ± 1.8	1.3 ± 0.7
E14		12 23 23.32	+15 51 29.6	14.9	9.4 ± 5.1	2.3 ± 1.2	2.9 ± 1.5	1.7 ± 0.8
E15 [c]	= H30	12 23 30.44	+15 45 06.5	49.1	59.0 ± 8.7	24.9 ± 2.1	31.9 ± 2.7	18.9 ± 1.4

[a] Fluxes are computed applying a 5 keV Raymond & Smith spectrum, assuming a hydrogen column density of $N_H = 2.3 \times 10^{20}$ cm^{-2}.
[b] ROSAT HRI fluxes and 3σ upper limits in the 0.1–2.4 keV band at the position of the *Einstein* sources.
[c] Only in the *Einstein* field of view for the 23.8 ks observation.

Table 4. ROSAT and *Einstein* point sources within the D_{25} ellipse of NGC 4321

Source		*Einstein* HRI (0.1–4.5 keV) F_x ($\frac{erg}{cm^2 s}$)	*Einstein* HRI (0.1–4.5 keV) L_x ($\frac{erg}{s}$)	ROSAT HRI (0.1–2.4 keV) F_x ($\frac{erg}{cm^2 s}$)	ROSAT HRI (0.1–2.4 keV) L_x ($\frac{erg}{s}$)	Location
H17		$< 6.9 \times 10^{-14}$	$< 2.4 \times 10^{39}$	3.6×10^{-14}	1.3×10^{39}	spiral arm
H18		$< 4.9 \times 10^{-14}$	$< 1.7 \times 10^{39}$	1.4×10^{-14}	4.9×10^{38}	interarm
H19	= E5	5.4×10^{-14}	1.9×10^{39}	1.2×10^{-14}	4.2×10^{38}	interarm
H21	= E4	1.2×10^{-13}	4.2×10^{39}	8.6×10^{-14}	3.0×10^{39}	bulge
H22		$< 6.9 \times 10^{-14}$	$< 2.4 \times 10^{39}$	1.4×10^{-14}	4.9×10^{38}	spiral arm
H23	= E7	1.4×10^{-13}	5.1×10^{39}	1.9×10^{-13}	6.5×10^{39}	NGC 4321 nucleus
H24		$< 2.9 \times 10^{-14}$	$< 1.0 \times 10^{39}$	1.7×10^{-14}	6.0×10^{38}	HII region CB 336 [a]
H25		$< 1.7 \times 10^{-13}$	$< 5.9 \times 10^{39}$	2.9×10^{-14}	1.0×10^{39}	SN 1979C

[a] Cepa & Beckman (1990)

rate for the complete observation. The count rates in the four time bins are consistent with a source of constant brightness (reduced $\chi^2 = 0.04$).

3.4. Diffuse X-ray emission

To investigate the diffuse emission component within NGC 4321, time intervals with a high particle background were rejected (remaining integration time 34.3 ks). An X-ray map was created using an adaptive filtering technique which enhances the signal-to-noise ratio for low surface brightness emission features (cf., e.g. Ehle, Pietsch & Beck 1995). The image was created with a pixel size of $6''.5$, and pixels of amplitude n were smoothed with a Gaussian of FWHM = $137 \times e^{0.35(1-n)}$. Pixels with an amplitude larger than 8 remained unsmoothed to ensure that bright point sources were not smeared into background regions (cf. Fig. 4).

Surface brightness profiles of NGC 4321 were constructed from an unfiltered low-background image with radial binning of $20''$ centered on the peak of the X-ray emission. The resulting radially binned surface brightness profiles for the total and the diffuse emission (excluding point sources listed in Table 2 to radii of twice the FWHM of the HRI PSF) are shown in Fig. 5.

A source-free region, well outside the D_{25} ellipse of the galaxy, was used to determine the mean background level. The residual emission count rate inside the D_{25} ellipse of the galaxy was calculated after subtraction of the mean background rate.

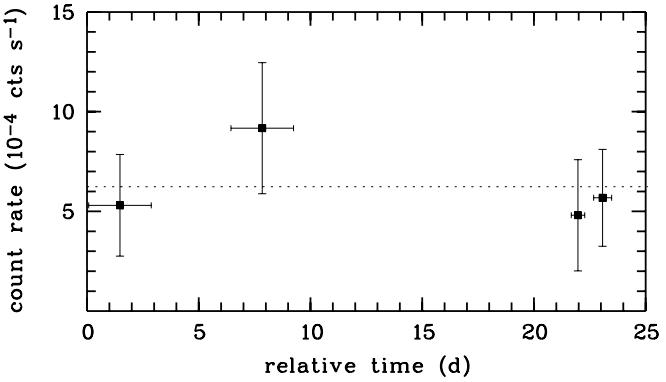

Fig. 3. X-ray lightcurve of SN 1979C. The 42.8 ks observation was binned into four observation blocks with integration times of $\sim$ 10 ks each. The horizontal error bars represent the time span of each binning in which the count rates were computed. Count rate errors correspond to $\pm 1\sigma$ statistical errors. The dotted horizontal bar gives the mean count rate in the complete observation.

Table 5. NGC 4321 emission components

Emission component	Count rate (10^{-3} s^{-1})	F_x ($\frac{\text{erg}}{\text{cm}^2\ \text{s}}$)	L_x ($\frac{\text{erg}}{\text{s}}$)
Total	37.1 ± 6.1	1.6×10^{-12}	5.5×10^{40}
Point sources (8)[a]	9.3 ± 1.3	0.4×10^{-12}	1.4×10^{40}
Bulge (< 1.2 kpc)[a]	7.1 ± 2.7	0.3×10^{-12}	1.1×10^{40}
Diffuse emission[b]	26.9 ± 5.2	1.0×10^{-12}	3.5×10^{40}

[a] F_x, L_x for a 5 keV thermal bremsstrahlung spectrum.
[b] F_x, L_x for a Raymond & Smith 3×10^6 K plasma.

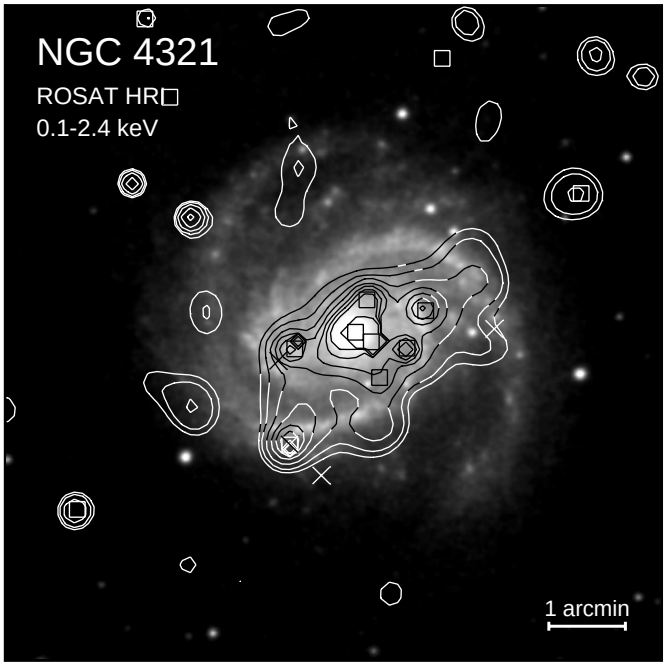

Fig. 4. Contour map of the ROSAT HRI image of NGC 4321 (0.1–2.4 keV) smoothed with an adaptive filter (FWHM $\leq 137''$, cf. Sect. 3.4) and superposed on a digitised Palomar Observatory Sky Survey plate. Contour levels are $3, 4, 6, 9, 13, 18, 24$ and 35σ above the background of 1.8×10^{-2} cts s^{-1} arcmin^{-2}. 1σ corresponds to 1.1×10^{-3} cts s^{-1} arcmin^{-2}. HRI sources are enclosed by boxes, positions of known SNe are marked with crosses. Same scale as Figs. 1 and 2.

Assuming the residual diffuse X-ray emission to have a spectrum of a hot (3×10^6 K), low-density plasma with cosmic abundances (cf., e.g. Raymond & Smith 1977 and Pietsch et al. 1994), fluxes and luminosities were calculated, taking galactic absorption into account. The energy conversion factor of 3.7×10^{-11} erg cm^{-2} cts^{-1} for 100% count detection transfers a count rate of 10^{-4} cts s^{-1} to a flux of 3.7×10^{-15} erg cm^{-2} s^{-1} and to a luminosity of 1.3×10^{38} erg s^{-1}. Luminosities for point sources were calculated assuming a 5 keV thermal bremsstrahlung spectrum. The results are listed in Table 5.

The *Einstein* observations were not used in the analysis of the diffuse emission due to the low response in the soft band and to background limitations.

4. Discussion

4.1. SN 1979C (H25)

SN 1979C, first observed in the optical by Johnson (1979) near maximum optical light ($m_B^{\max} \leq 12$), on April 19, 1979, is thought to have exploded on April 4, 1979 (Weiler et al. 1986). Extensive studies in the optical, radio and ultraviolet over subsequent years revealed that SN 1979C was of type II_L ('linear' subclass with a small rate of decline in the radio of $t^{-0.7}$), originated from a high-mass red supergiant progenitor ($M_{\text{ZAMS}} \gtrsim 13 M_\odot$) with a shell expansion velocity of $\sim 9\,000$ km s^{-1} near maximum (cf., e.g. Panagia et al. 1980, Branch et al. 1981, de Vaucouleurs et al. 1981, Fransson et al. 1984, Weiler et al. 1986, 1991 and Fesen & Matonick 1993). In the radio regime, SN 1979C was first detected one year after it's outburst ($f_{6\text{cm}} = 5$ mJy, Weiler et al. 1981) and showed a maximum radio flux density of $f_{6\text{cm}}^{\max} = 8.3$ mJy some weeks later. Radio emission at longer wavelengths reached its peak three years after the outburst ($f_{20\text{cm}}^{\max} \sim 13$ mJy, Weiler et al. 1986).

X-ray observations with the *Copernicus* satellite (Panagia et al. 1980) and the *Einstein* Observatory (Palumbo et al. 1981) succeeded only in establishing an upper limit to the X-ray flux from SN 1979C. The 3σ confidence level upper limit for the December 1979 *Einstein* HRI observation is estimated to be $L_x < 8.8 \times 10^{39}$ erg s^{-1} (corrected to a distance of 17.1 Mpc).

SN 1979C is detected by the ROSAT HRI with a luminosity of $L_x = 1.0 \times 10^{39}$ erg s^{-1} 16.2 years after the explosion. The 3σ upper limit of the merged 41.3 ks *Einstein* observations, taken between days 64 and 454 after the explosion, is 5.9×10^{39} erg s^{-1}, assuming a 5 keV Raymond & Smith plasma spectrum. We derive upper limits for the individual *Einstein* observations, taken on days 64, 239 and 454 after the outburst, of

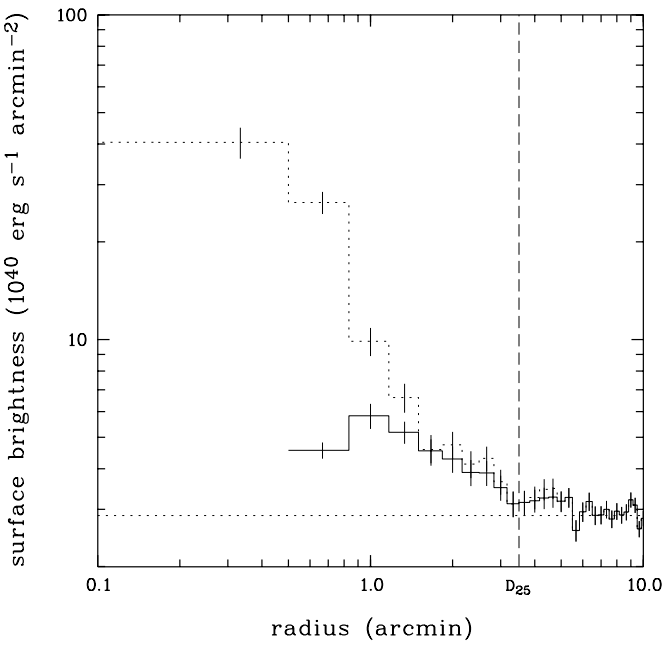

Fig. 5. Radial surface brightness profile of the X-ray emission from NGC 4321, centered on the optical nucleus. The dotted line shows the radially-binned surface brightness profile of the total emission of NGC 4321 (including point sources), the solid line represents the diffuse emission (excluding point sources according to Table 2). The mean background level of 2.87×10^{40} erg s^{-1} arcmin^{-2} is indicated by a dotted horizontal line, the D_{25} radius of the galaxy is given by a vertical dashed line.

1.8×10^{40} erg s^{-1}, 7.6×10^{39} erg s^{-1} and 6.9×10^{39} erg s^{-1}, respectively.

The upper limits to the luminosity for the early epochs and the measurement 16 years after are surprisingly close to each other, indicating little long-term variation of at least the X-ray flux. It has been proposed that X-rays from type II supernovae are created by the interaction of the supernova gas with the circumstellar medium, which is likely to be the wind blown by the progenitor star prior to the explosion (Chevalier 1982a,b, 1984a,b, Chevalier & Fransson 1994). The circumstellar matter is heated by the outgoing shock wave associated with the explosion, the supernova gas is heated by the reverse shock wave and the entire matter is confined in a shell. This sometimes called 'mini-shell' model has successfully been used to explain the radio emission from type II supernovae. The radial supernova gas profile is approximated by a power law, $\rho_{\rm SN} \sim r^{-\rm n}$ and the density distribution of the circumstellar matter is $\rho_{\rm w} \sim r^{-2}$. Both radio and X-ray luminosity depend on the shocked matter density, which is proportional to the mass loss rate $\dot{\rm M}$ of the progenitor star divided by the wind velocity $\rm v_w$, assuming a constant $\rm v_w$. The supernova shock front radius increases with time as $\rm t^m$ with m = (n-3)/(n-2) (Chevalier & Fransson 1994). The change in radius with time is reflected in the radio and X-ray light curves, and Weiler et al. (1991) have used the 10 year radio light curve of SN 1979C to determine $\dot{\rm M}/{\rm v_w} = 12$, with $\dot{\rm M}$ in units of 10^{-5} solar masses per year, and $\rm v_w$, measured in 10 km/s (see also Lundqvist & Fransson 1988). The index m has been determined to be very close to unity, which means that n is large, and the best fit to the radio light curve by Weiler et al. gives n = 79 with a lower limit of n > 22 (cf. Chevalier & Fransson 1994). We have used these values to determine the X-ray luminosity expected from the circumstellar interaction model, and it turns out that the ROSAT measurements give a luminosity at least a factor of 30 lower than the model predicts. Such an excess predicted by the model has already been noted for the early *Einstein* upper limits by Chevalier & Fransson (1994). They have proposed that photoelectric absorption of the reverse shock X-rays by an outer cool shell could bring together measurement and prediction, but this is not likely to happen at the time of the ROSAT measurements because of the dilution of the shell density and the corresponding low column density. A detailed discussion of the X-ray data with respect to the circumstellar interaction model is beyond the scope of this paper and is presented in a separate publication (Aschenbach, Immler & Pietsch 1997). Clearly, further X-ray data are needed, and we are looking forward to further X-ray observations of NGC 4321, both with ROSAT and other X-ray observatories, to monitor the X-ray lightcurve of SN 1979C and to obtain spectra.

No significant X-ray emission is detected from the type I supernovae SN 1901B, SN 1914A and SN 1959E. 3σ upper limits were calculated within circles of radius $2.5\times$ the ROSAT HRI PSF at these SNe positions. The upper limits are listed in Table 6 together with the 3σ upper limits from the merged 41.3 ks *Einstein* observations. The luminosities are less than a few $\times 10^{38}$ erg s^{-1} for all of the type I SNe. This is consistent with the circumstellar interaction model, since type Ia supernovae are not expected to be surrounded by sufficiently dense matter because the progenitor is a white dwarf (cf., e.g. Schlegel 1995, Branch et al. 1995, Cumming et al. 1996). In case of SN 1901B, SN 1914A and SN 1959E, any ambient matter would be required to have a density comparable within a factor of 3 to that surrounding SN 1979C in order for them to exceed the ROSAT detection threshold.

4.2. Point sources outside the D_{25} ellipse of NGC 4321

Within the $34' \times 34'$ ROSAT HRI field of view, a total of 25 point-like X-ray sources with a likelihood $L \geq 8$ are detected outside the D_{25} ellipse of the galaxy. The *Einstein* observations lead to the detection of nine point sources with $L \geq 8$ outside the D_{25} ellipse of the galaxy, five of which correspond to ROSAT sources.

Source H8 is $8\farcm9$ offset from the pointing direction of the ROSAT observation. The X-ray flux in the 0.1–2.4 keV band is 2.6×10^{-13} erg cm^{-2} s^{-1}. Comparison with the APM finding charts (Irwin et al. 1994) suggests an identification of H8 with a faint stellar object $2\farcs6$ offset from the X-ray position ($m_{\rm B} = 19.99$, $m_{\rm R} = 19.14$, $m_{\rm B} - m_{\rm R} = 0.85$). The source is the brightest X-ray source both in the ROSAT and in the merged *Einstein* HRI observations. A lower (0.1–4.5 keV) X-ray flux of 1.8×10^{-13} erg cm^{-2} s^{-1} is seen during the *Einstein* ob-

Table 6. X-ray properties of SNe in NGC 4321

Supernova	R.A. (J2000) (^{h} ^{m} ^{s})	Dec. (J2000) ($^\circ$ $'$ $''$)	*Einstein* HRI (0.1–4.5 keV) L_x[a] ($\frac{erg}{s}$) (13 ks)	*Einstein* HRI (0.1–4.5 keV) L_x[b] ($\frac{erg}{s}$) (41 ks)	ROSAT HRI (0.1–2.4 keV) F_x[c] ($\frac{erg}{cm^2\ s}$) (42.8 ks)	ROSAT HRI (0.1–2.4 keV) L_x[c] ($\frac{erg}{s}$) (42.8 ks)
SN 1901B	12 22 47.48	+15 49 24.6	$< 7.3 \times 10^{39}$	$< 4.8 \times 10^{39}$	$< 5.0 \times 10^{-15}$	$< 1.8 \times 10^{38}$
SN 1914A	12 22 56.85	+15 47 29.6	$< 1.1 \times 10^{40}$	$< 4.4 \times 10^{39}$	$< 5.0 \times 10^{-15}$	$< 1.8 \times 10^{38}$
SN 1959E	12 22 59.20	+15 48 59.6	$< 6.9 \times 10^{39}$	$< 3.6 \times 10^{39}$	$< 7.9 \times 10^{-15}$	$< 2.7 \times 10^{38}$
SN 1979C	12 22 58.62	+15 47 50.7	$< 8.8 \times 10^{39}$	$< 5.9 \times 10^{39}$	2.9×10^{-14}	1.0×10^{39}

[a] *Einstein* HRI 3σ upper limit (Palumbo et al. 1981) corrected for a distance of 17.1 Mpc.
[b] *Einstein* HRI 3σ upper limit (this work) within a circle of $18''$ radius.
[c] ROSAT HRI 3σ upper limit in a circle with radius 2.5× the HRI PSF.

servations. No variability is observed throughout the ROSAT observation.

H30 is the second brightest X-ray source in the ROSAT observation ($F_x = 1.9 \times 10^{-13}$ erg cm^{-2} s^{-1}) $14'$ offset from the pointing direction. The source is in the field of view only in the 24 ks *Einstein* observation (E15, $F_x = 3.2 \times 10^{-13}$ erg cm^{-2} s^{-1}) as the three *Einstein* observations do not overlap entirely. Timing analysis of the ROSAT data shows a variation in count rate over the observation period by a factor of ~ 4.5. A faint non-stellar object ($m_B = 17.54$, $m_R = 16.38$, $m_B - m_R = 1.16$) is seen $2\farcs5$ offset from the X-ray position in the APM finding charts, suggesting the X-ray source being a variable AGN.

H12 at the D_{25} ellipse of NGC 4321 is $7\farcs2$ offset from the *Einstein* source E3. A faint blue non-stellar object ($m_B = 21.83$, $m_B - m_R < 1.83$) is located $8\farcs2$ offset from the ROSAT and $1\farcs8$ offset from the *Einstein* positions. The X-ray source is slightly brighter in the (harder) *Einstein* band ($F_x = 4.1 \times 10^{-14}$ erg cm^{-2} s^{-1}) compared to the ROSAT band (1.0×10^{-14} erg cm^{-2} s^{-1}) and suggests an identification with an AGN not associated with NGC 4321.

All the other *Einstein* sources outside the D_{25} ellipse of NGC 4321 (E2, E10, E11/H27, E12/H28, E13, E14) are observed to have slightly higher *Einstein* band fluxes ($2.9 - 4.9 \times 10^{-14}$ erg cm^{-2} s^{-1}) compared to the ROSAT observation ($0.9 - 1.5 \times 10^{-14}$ erg cm^{-2} s^{-1}). No optical identifications are found within the errors of the X-ray positions.

4.3. Point sources within the D_{25} ellipse of NGC 4321

Seven additional ROSAT point sources with a likelihood $L \geq 8$ are detected inside the D_{25} ellipse of NGC 4321, with luminosities in the range 4.2×10^{38} to 6.5×10^{39} erg s^{-1}, well in excess of the Eddington limit for an accreting binary. These sources may be explained either by accretion onto a massive black hole or onto a $1 M_\odot$ magnetised neutron star or by a collection of unresolved, weak sources.

Alternatively, these bright X-ray sources may be due to previously unrecorded SNe. Based on the estimated SN rate of 1.3 ± 0.3 per century per 10^{10} $L_B(\odot)$ for galaxies of type Sab – Sd (van den Bergh 1993) and a total blue luminosity of NGC 4321 of 6.9×10^{10} $L_B(\odot)$ (Shostak 1978), a SN rate of ~ 10 per century is expected within NGC 4321. This is similar to the SN rate derived for M 51 (Marston et al. 1995) which is a factor of ~ 3 higher than in our own Galaxy ($\sim 3 \pm 1$ per century, van den Bergh 1993). It is therefore conceivable that up to ~ 10 SN explosions occurred in NGC 4321 over the last century, some of which may have evolved into the observed bright X-ray point sources.

H23, at the optical and radio position of the NGC 4321 nucleus, is the brightest X-ray source in the galaxy ($L_x = 6.5 \times 10^{39}$ erg s^{-1}). It is the only source flagged as extended by the source detection algorithm and consequently, it is difficult to separate from the surrounding diffuse X-ray emission. The X-ray lightcurve shows marginal evidence for small variations in the count rate by a factor of ~ 1.4 (reduced $\chi^2 = 1.24$) throughout the observation period. This suggestion of variability is strengthened by the lower luminosity observed with *Einstein* (E7, 5.1×10^{39} erg s^{-1}).

One additional bright point source is detected within a radius of $15''$ ($\widehat{=}$ 1.2 kpc) from the nucleus (H21, 3.0×10^{39} erg s^{-1}). Timing analysis shows variations in the count rate by a factor of ~ 1.7 (reduced $\chi^2 = 1.17$) during the ROSAT observation and a higher luminosity in the *Einstein* 0.1–4.5 keV band (E4, 4.2×10^{39} erg s^{-1}).

The bulge sources (H21 and H23) are considerably brighter than the brightest nuclear sources found in M 31 ($L_x \sim 2 \times 10^{38}$ erg s^{-1}, Primini, Forman & Jones 1993, Supper et al. 1997). In the optical and radio regimes NGC 4321 displays violent nuclear activity with a sharp increase in the star formation rate within the central 500 pc and indicate the presence of a bar and a dust obscured AGN (Knapen et al. 1993, Knapen et al. 1995a, 1995b, Sakamoto et al. 1995). The observations in the X-ray domain confirm the existence of nuclear activity and point towards NGC 4321 being a galaxy intermediate between that of normal and AGN-type systems.

A southern interarm source (H19/E5) is the third X-ray source detected inside the NGC 4321 D_{25} ellipse in the merged *Einstein* observations and in the ROSAT observation. The source has an *Einstein* luminosity of 1.9×10^{39} erg s^{-1}, well

in excess of the ROSAT value of $L_x = 4.2 \times 10^{38}$ erg s^{-1}. No variability could be ascertained from the ROSAT observation.

H24 is at the position of a bright HII region in the eastern spiral arm (CB 336, Cepa & Beckman 1990). The X-ray source is slightly extended and its morphology closely follows the Hα emission. The high Hα luminosity ($-2.5 \log f_{H\alpha} = -11.8$), the size of the HII region (26.5 arcsec^2) and the X-ray luminosity ($L_x^{ROSAT} = 6.0 \times 10^{38}$ erg s^{-1}, $L_x^{Einstein} < 1.0 \times 10^{39}$ erg s^{-1}) show that the region is similar to X-ray emitting HII regions in M 101 (NGC 5447, NGC 5455, NGC 5461, NGC 5462, NGC 5471) and to 30 Dor in the LMC (Williams & Chu 1995). Each of the HII regions in M 101 contains a variety of source components such as SNRs, hot X-ray emitting gas at a temperature of some 10^6 K with soft X-ray spectra, and X-ray binaries, suggesting that the X-ray emission of H24 is associated with hot gas in the HII region and several unresolved point sources.

The previously reported *Einstein* source in the northern spiral arm (1E 122022+1606.8, $F_x = 3.7 \times 10^{-13}$ erg cm^{-1} s^{-1}, $L_x = 1.1 \times 10^{40}$ erg s^{-1} corrected to a distance of 17.1 Mpc, Palumbo et al. 1981) is considerably fainter in the merged 41 ks *Einstein* HRI observations, and is only detected at the 3σ level ($F_x = 5.9 \times 10^{-14}$ erg cm^{-1} s^{-1}, $L_x = 2.1 \times 10^{39}$ erg s^{-1}). This source is not detected in the ROSAT HRI observation, its 3σ upper limit being $F_x < 8.0 \times 10^{-15}$ erg cm^{-1} s^{-1} in the ROSAT 0.1–2.4 keV band. This might be suggestive of the X-ray emission recorded in the 13 ks *Einstein* HRI observation from Dec. 10, 1979, being due to a bright transient outburst.

In summary, the ROSAT and *Einstein* results for point sources lead to eight ROSAT sources inside the D_{25} ellipse of NGC 4321 with luminosities ranging from 4.2×10^{38} – 6.5×10^{39}erg s^{-1} and six *Einstein* sources in the range 1.1 – 5.1×10^{39}erg s^{-1}. The sources radiate well in excess of the Eddington limit for a $1M_\odot$ accreting binary and can be explained either by accretion, either onto a massive black hole or onto a $1M_\odot$ magnetised neutron star, or by a number of spatially unresolved weak sources. Alternatively, the X-ray sources could be attributed to previously unrecorded SN explosions. The high expected SN rate in NGC 4321 ($\sim$ 10 per century) and the constant count rate of the X-ray sources support the assumption that a fraction of the X-ray sources is associated with previously unrecorded SNe. The two brightest *Einstein* sources in NGC 4321 are coincident with the bulge sources detected in the ROSAT observation (H21/E4, H23/E7). Timing analysis and comparison of the luminosities in the ROSAT and *Einstein* observations indicate that the sources are variable. The violent nuclear activity, as observed in the optical and radio regimes, points to NGC 4321 being a galaxy intermediate between normal and AGN-type systems, a point endorsed on the basis of the X-ray observations. One *Einstein* source coincides with a ROSAT southern interarm source observed to have a significant higher luminosity (H19/E5). The low ROSAT upper limits for the remaining *Einstein* sources suggest that these sources are transients or variable AGN detected with the *Einstein* Observatory. The ROSAT source H24 coincides with the position of a bright HII region similar in luminosity and optical size to previously detected X-ray bright HII regions in other spiral galaxies.

4.4. Diffuse X-ray emission

Diffuse emission is visible over the entire optical extent of the galaxy (cf. Figs. 4 and 5) and contributes $\sim$ 60% (3.5×10^{40} erg s^{-1}) to the total luminosity of NGC 4321 inside the D_{25} ellipse (5.5×10^{40} erg s^{-1}, cf. Table 5).

Evidence for a diffuse X-ray emission component extending to large radii has been found in other face-on spiral galaxies of type Sb,c, too, including M 51 (luminosity of the diffuse component in the ROSAT band 1.5×10^{40} erg s^{-1}, Ehle, Pietsch & Beck 1995), M 83 (3.6×10^{40} erg s^{-1}, Ehle et al. 1997), M 101 (3.6×10^{39} erg s^{-1} in the $\frac{3}{4}$ keV and 1.5 keV band and 10^{40} – 10^{41} erg s^{-1} in the $\frac{1}{4}$ keV band, Snowden & Pietsch 1995) and NGC 1566 (1.4×10^{40} erg s^{-1}, Ehle et al. 1996). The diffuse component in these galaxies is thought to originate from a hot ($\sim 10^6$ K) gaseous halo above the galactic plane. Regions confined inside the disk are unlikely to account for the emission since the required filling factors are very large and the required low temperatures contradict the measured values. The anti-correlation of the X-ray emitting regions and the polarised radio emission in the inner spiral arms of M 51 and M 83 is probably indicative of outflowing material from the galactic disk into the halo, driven by an enhanced star formation rate.

It can be seen that the X-ray luminosity of the diffuse emission in NGC 4321 is similar to that of M 51, M 83, M 101 and NGC 1566, though these galaxies' diffuse components attain significantly higher luminosities when compared to edge-on galaxies, a fact partly due to the geometry of the line of sight with a minimum absorption in the galactic disks. The unresolved emission, however, is more confined to the inner spiral arms of NGC 4321 (cf. Fig. 4), similar to NGC 1566. The diffuse X-ray emission covers the same area for which Sakamoto et al. (1995) report the detection of strong CO emission. This might be suggestive of a star-formation driven outflow into the galactic halo via galactic fountains (Norman & Ikeuchi 1989). Future X-ray observations with spectral information are required in order to address the nature of the unresolved diffuse emission component.

Acknowledgements. We thank Andreas Vogler for fruitful discussions, Andy Read for reading the manuscript and our colleagues from the MPE ROSAT group for their support. This research has made use of the SIMBAD database operated at CDS, Strasbourg, the EINLINE online archive at the Smithsonian Astrophysical Observatory and the Digitized Sky Survey based on photographic data of the National Geographic Society – Palomar Observatory Sky Survey. The Digitized Sky Survey was produced at the Space Telescope Science Institute under US Government grant NAG W-2166. The ROSAT project is supported by the German Bundesministerium für Bildung, Wissenschaft, Forschung und Technologie (BMBF/DARA) and the Max-Planck-Gesellschaft (MPG).

References

Aschenbach, B., Immler, S., Pietsch, W., 1998, in preparation
van den Bergh, S., 1993, Comments on Astrophys. 17, 125
Branch, D., Falk, S.W., McCall, M.L., et al., 1981, ApJ 244, 780
Branch, D., Livio, M., Yungelson, L.R., et al., 1995, PASP 107, 1019

Cepa, J., Beckman, J.E., 1990, A&AS 83, 211
Chevalier, R.A., 1982a, ApJ 258, 790
Chevalier, R.A., 1982b, ApJ 259, 302
Chevalier, R.A., 1984a, ApJ 285, L63
Chevalier, R.A., 1984b, Ann. NY Acad. Sci. 422, 215
Chevalier, R.A., Fransson, C., 1994, ApJ 420, 268
Cumming, R.J., Lundqvist, P., Smith, L.J., et al., MNRAS 283, 1355
Dickey, J.M., Lockman, F.J., 1990, ARA&A 28, 215
Ehle, M., Pietsch, W., Beck, R., 1995, A&A 295, 289
Ehle, M., Beck, R., Heynes, R.F., et al., 1996, A&A 306, 73
Ehle, M., Pietsch, W., Beck, R., et al., 1998, A&A 329, 39
Fabbiano, G., 1989, ARA&A 27, 87
Fesen, R.A., Matonick, D.M., 1993, ApJ 407, 110
Fransson, C., Benvenuti, P., Wamsteker, W., et al., 1984, A&A 132, 1
Freedman, W.L., Madore, B.F., Mould, J.R., et al., 1994, Nat 371, 757
Harris, D.E., 1984, *Einstein* Observatory Revised User's Manual
Hasinger, G., Schmidt, M., Trümper, J., 1991, A&A 246, L2
Irwin, M., Maddox, S., McMahon, R., 1994, Spectrum 2, 14
Johnson, G.E., 1979, IAU Circ., No. 3348
Knapen, J.H., Cepa, J., Beckman, J.E., et al., 1993, ApJ 416, 563
Knapen, J.H., Beckman, J.E., Heller, C.H., et al., 1995a, ApJ 454, 623
Knapen, J.H., Beckman, J.E., Shlosman, I., et al., 1995b, ApJ 443, L73
Lundqvist, P., Fransson, C., 1988, A&A 192, 221
Marston, A.P., Elmegreen, D., Elmegreen, B., et al., 1995, ApJ 438, 663
Norman, C.A., Ikeuchi, S., 1989, ApJ 345, 372
Palumbo, G.G.C., Maccacaro, T., Zamorani, G., et al., 1981, ApJ 247, 484
Panagia, N., Vettolani, G., Boksenberg, A., et al., 1980, MNRAS 192, 861
Penhallow, W.S., 1980, IAU Circ., No. 3491
Pietsch, W., Vogler, A., Kahabka, P., et al., 1994, A&A 284, 386
Primini, F.A., Forman, W., Jones, C., 1993, ApJ 410, 615
Raymond, J.C., Smith, B.W., 1977, ApJS 35, 419
Sakamoto, K., Okumura, S., Minezaki, T., et al., 1995, AJ 110, 2075
Schlegel, E.M., 1994, AJ 108, 1893
Schlegel, E.M., 1995, Rep. Prog. Phys. 58, 1375
Shostak, G.S., 1978, A&A 68, 321
Snowden, S.L., Pietsch, W., 1995, ApJ 452, 627
Supper, R., Hasinger, G., Pietsch, W., et al., 1997, A&A 317, 328
Trümper, J., 1983, Adv. Space Res. 2, 241
de Vaucouleurs, G. de Vaucouleurs, A., Buta, R., et al., 1981, PASP 93, 36
de Vaucouleurs, G., de Vaucouleurs, A., Corwin, H.G.C, et al., 1991, Third Reference Catalogue of Bright Galaxies, Springer, New York
Voges, W., et al., 1992, in: Guyenne, T.D., Hunt, J.J. (eds.), Proc. European ISY conference, ESA ISY-3, 223
Vogler, A., Pietsch, W., 1996, A&A 311, 35
Weiler, K.W., van der Hulst, J.M., Sramek, R.A., et al., 1981, ApJ 243, L151
Weiler, K.W., Sramek, R.A., Panagia, N., et al., 1986, ApJ 301, 790
Weiler, K.W., van Dyk, S.D., Discenna, J.L., et al., 1991, ApJ 380, 161
Williams, R.M., Chu, Y.-H., 1995, ApJ 439, 132
Zimmermann, H.-U., Becker, W., Belloni, T., et al., 1994, EXSAS User's Guide, 4th edition, MPE Report 257

This article was processed by the author using Springer-Verlag LaTeX A&A style file *L-AA* version 3.